



Linking Cause and Effect: Nanoscale Vibrational Spectroscopy of Space Weathering from Asteroid Ryugu

Sylvain Laforet¹ , Corentin Le Guillou¹, Francisco de la Peña¹, Michael Walls², Luiz H. G. Tizei², Maya Marinova³, Pierre Beck⁴, Van T. H. Phan⁴, Damien Jacob¹, Bahae-eddine Mouloud¹, Daniel Hallatt^{1,5} , Mario Pelaez-Fernandez^{1,6}, Jean-Christophe Viennet¹, David Troadec⁷, Takaaki Noguchi⁸ , Toru Matsumoto^{8,9}, Akira Miyake⁸, Hisayoshi Yurimoto¹⁰ , and Hugues Leroux¹

¹ Université de Lille, CNRS, INRAE, Centrale Lille, UMR 8207-UMET-Unité Matériaux et Transformations, F-59000 Lille, France

² Université Paris-Saclay, CNRS, Laboratoire de Physique des Solides, 91405 Orsay, France

³ Université de Lille, CNRS, INRAE, Centrale Lille, Université Artois, FR 2638-IMEC-Institut Michel-Eugène Chevreul, F-59000 Lille, France

⁴ Université de Grenoble Alpes, CNRS, IPAG, 38000 Grenoble, France

⁵ Department of Physics and Astronomy, University of Kent, Canterbury, Kent CT2 7NH, UK

⁶ Instituto de Nanociencia y Materiales de Aragón, CSIC- Universidad de Zaragoza, Zaragoza, Spain

⁷ Université de Lille, CNRS, Centrale Lille, Junia, Univ. Polytechnique Hauts-de-France, UMR 8520—IEMN - Institut d'Electronique de Microélectronique et de Nanotechnologie, F-59000 Lille, France

⁸ Division of Earth and Planetary Sciences, Kyoto University, Kitashirakawa-iwake-cho, Sakyo-ku, Kyoto 606-8502, Japan

⁹ The Hakubi Center for Advanced Research, Kyoto University, Kitashirakawa-iwake-cho, Sakyo-ku, Kyoto 606-8502, Japan

¹⁰ Department of Earth and Planetary Sciences, Hokkaido University, Kita-10 Nishi-8, Kita-ku, Sapporo 060-0810, Japan

Received 2023 December 20; revised 2024 February 19; accepted 2024 February 19; published 2024 March 8

Abstract

Airless bodies are subjected to space-weathering effects that modify the first few microns of their surface. Therefore, understanding their impact on the optical properties of asteroids is key to the interpretation of their color variability and infrared reflectance observations. The recent Hayabusa2 sample return mission to asteroid Ryugu offers the first opportunity to study these effects, in the case of the most abundant spectral type among the main-asteroid belt, C-type objects. This study employs vibrational electron energy-loss spectroscopy in the transmission electron microscope to achieve the spatial resolution required to measure the distinct mid-infrared spectral signature of Ryugu's space-weathered surface. The comparison with the spectrum of the pristine underlying matrix reveals the loss of structural -OH and C-rich components in the space-weathered layers, providing direct experimental evidence that exposure to the space environment tends to mask the optical signatures of phyllosilicates and carbonaceous matter. Our findings should contribute to rectifying potential underestimations of water and carbon content of C-type asteroids when studied through remote sensing with new-generation telescopes.

Unified Astronomy Thesaurus concepts: [Space weather \(2037\)](#); [Asteroid surfaces \(2209\)](#); [Remote sensing \(2191\)](#); [Small Solar System bodies \(1469\)](#); [Vibrational spectroscopy \(2249\)](#); [Infrared spectroscopy \(2285\)](#); [Impact gardening \(2299\)](#); [Planetary mineralogy \(2304\)](#)

1. Introduction

Our understanding of the origin and evolution of the asteroid belt relies on a combination of constraints on asteroid dynamics and compositions. As of today, for the vast majority of asteroids, the only constraints on composition available are reflected sunlight observations in the visible and infrared, which are at the core of asteroid taxonomic classification (Rivkin et al. 2015, 2016; Thomas et al. 2016; Mählke et al. 2022). However, only a few compounds or atoms have absorptions in the visible and near-infrared range, and the interpretation of reflectance spectra strongly relies on comparison to known extraterrestrial asteroid samples. Another challenge resides in the fact that reflectance spectra only probe the very surface of the objects (typically a few to several tens of microns), and are therefore highly sensitive to the set of processes occurring at the surface of airless bodies, namely space weathering.

It has been clearly recognized now that solar wind irradiation and high-velocity micrometeorite bombardments generate

strong surface modifications, often hindering the identification of asteroid mineralogy by remote sensing (Hapke 2001; Chapman 2004; Pieters & Noble 2016). So far, the effects of space weathering have been extensively investigated on two anhydrous airless bodies, the Moon and the S-type asteroid Itokawa (Keller & McKay 1997; Pieters et al. 2000; Noguchi et al. 2011, 2014; Thompson et al. 2014; Brunetto et al. 2015; Pieters & Noble 2016; Matsumoto et al. 2021). In both cases the space-weathered product is a thin layer (~ 100 nm) of amorphous silicate containing metallic iron nanophases (npFe⁰). From an optical point of view, these phases modify the reflectance properties, such as band depth and position, albedo, and spectral slope (Pieters & Noble 2016).

Recently, the sample return mission Hayabusa2, conducted by the Japan Aerospace Exploration Agency (JAXA), recently brought back to Earth 5.4 g from the surface of the carbonaceous (Cb-type) asteroid Ryugu. The porous, airless, hydrated and carbon-rich asteroid has likely reassembled from fragments of a previous parent body in the main asteroid belt (Watanabe et al. 2019; Michel et al. 2020; Ito et al. 2022; Yokoyama et al. 2023). Remote and laboratory measurements have revealed that Ryugu's surface exhibits extremely low reflectance and weak absorption features at 2.7 and 3.4 μm , attributed to a carbon-rich nature and the presence of secondary

alteration phases (Kitazato et al. 2019, 2021; Nakamura et al. 2023). Pilorget et al. (2022) and Matsuoka et al. (2023) highlighted important differences between Hayabusa2's remote measurements (Kitazato et al. 2019) and Ryugu laboratory spectra. In particular, the band depth of the 2.7 μm absorption, assigned to the hydroxyl group (-OH) in phyllosilicates, happens to be 2 times lower in remote sensing spectra.

Ryugu's mineralogy consists of a phyllosilicate-rich matrix (serpentine and saponite), which represents about 70 vol% of the total mineralogy (Nakamura et al. 2023), complemented with Fe-Ni-sulfides, magnetites, carbonates, and phosphates. It is similar to that of Ivuna-like carbonaceous chondrites (Ito et al. 2022; Nakamura et al. 2023; Yada et al. 2022; Yokoyama et al. 2023; Leroux et al. 2023), which are the most primitive chondrites and have a composition almost identical to that of the bulk solar system (Lodders 2003).

Noguchi et al. (2022, 2023) and Matsumoto et al. (2024) have observed unique features not previously observed in meteorites, including particular surface textures attributed to space weathering. They consist in a submicrometer sized assemblage of glassy silicates containing vesicles and nano-sulfides that are draping the surface of typical phyllosilicate-rich Ryugu grains. Establishing a connection between remote sensing data (obtained at the millimeter to kilometer scale) and these nanometer-scale textures requires characterization techniques capable of measuring the spectral signature of Ryugu's space-weathered regions at submicrometer spatial resolution. Recently, new infrared techniques have been developed to overcome the diffraction limit, such as Nano-FTIR (Herman 2013; Kebukawa et al. 2019; Yesiltas et al. 2021) or photothermal atomic force microscopy-based infrared spectroscopy (AFM-IR; Dazzi & Prater 2017; Kebukawa et al. 2019; Mathurin et al. 2019, 2022; Phan et al. 2022; Dartois et al. 2023; Phan et al. 2023). Both techniques can reach 50 nm spatial resolution with $\sim 8 \text{ cm}^{-1}$ spectral resolution typically between 700 and 2000 cm^{-1} (Phan et al. 2023). Unfortunately, the application of these techniques to Ryugu samples is difficult due to sample preparation issues. Indeed, isolating the signature of the space-weathered layer from the unweathered matrix requires the extraction of a cross section from the fragment containing the melt layer. This can currently only be accomplished by focused ion beam (FIB) techniques, which are at the time challenging to combine to for AFM-IR and Nano-FTIR measurements due to the high fragility of Ryugu samples.

Fortunately, a new generation of monochromated scanning transmission electron microscopes (STEMs) can acquire electron energy-loss (EELS) spectra with an energy resolution greater than 4.8 meV (40 cm^{-1}), enabling vibrational spectroscopy at nanometric spatial resolution (Krivanek et al. 2014; Jokisaari et al. 2018; Hage et al. 2020; Colliex 2022). This technique offers the possibility to cover a wide spectral range, from 80 meV (15 μm) and up to few eV ($\sim 1 \mu\text{m}$). So far, vibrational STEM-EELS has barely been used to study extraterrestrial materials (Stroud et al. 2019; Vollmer et al. 2019). In addition, this technique has the advantage that multiple other analysis can be performed by the same instrument, such as imaging, energy dispersive X-ray spectroscopy (EDXS), scanning electron diffraction, cathodoluminescence, and conventional EELS.

In this context, we report the nanoscale analysis of space-weathered Ryugu grains. Using vibrational-EELS, we separate

the mid-infrared (MIR; 2.5–12 μm) spectral signature of Ryugu space-weathered layers from the unweathered underlying matrix. By comparing vibrational-EELS with millimetric grain FTIR spectra in the MIR, we unveil the effects of space weathering's alteration on the optical properties of a hydrated C-type asteroid.

2. Materials and Methods

Ryugu grains first look. JAXA allocated samples of their Hayabusa2 space mission to the University of Lille (France). Both small grains (typically $\sim 50 \mu\text{m}$ diameter) and thin transmission electron microscopy (TEM) sections were received and analyzed. The Ryugu grains were collected in chamber C of Hayabusa2 spacecraft, during the second touch-down sampling (Tsuda et al. 2020). They were disposed and glued on a Au plate with epoxy resin (C0105-034). Space-weathered grains, characterized by smooth and/or vesiculated surfaces, were identified using a JEOL JSM-7800F LV SEM, operating at 4 kV.

FIB preparation performed in Lille (IEMN), France. Thin foils sections were extracted from grains of the plate C0105-034 by FIB. The preparation was performed using a dual-beam Thermo Fisher Strata DB235. The electron beam source is a field emission gun (FEG), and the ion source is a liquid/metal gallium. Before the thin foil extraction, the chosen areas were covered with a Pt-C layer for protection. The first part of the extraction process was performed with a 10 nA probe current at 15 kV. The final thinning process was done with a 50 pA probe current at 5 kV in order to minimize redeposition and amorphization, and to obtain a homogeneous thickness of the final FIB sections.

FIB sections of the phyllosilicate reference sample were extracted from SARM (Serpentine UB-N) and from Clay Minerals Society (Saponite SapCa-2). The FIB section from the Orgueil CI chondrite was extracted from a millimetric grain using the same preparation protocol.

FIB preparation performed in Kyoto, Japan. The FIB section received from JAXA, A0058-C2001-02 (collection chamber A) (Tsuda et al. 2020), was prepared at the Kyoto University as follows. First, grain A0058's surface morphology was observed using a JEOL JSM-7001F FE-SEM, with a 15 pA current and a 2 kV acceleration voltage. The A0058-C2001-02 FIB section was prepared using a Thermo Fisher Helios G3 CX FIB-SEM. The selected area was cut out with a 30 kV Ga^+ ion beam. Before the extraction, the targeted surface was Pt-C coated by a 2 kV electron beam. Then, Pt-C was deposited on the target areas with 30 kV Ga^+ ion beams. The section mounted on the TEM grid was thinned to a thickness of $\sim 150 \text{ nm}$ using 16 or 30 kV Ga^+ ion beams. The damaged layers were removed using a 2 kV Ga^+ ion beam (Noguchi et al. 2022).

Orgueil IOM thin sample preparation. Orgueil insoluble organic matter (IOM) thin sample were prepared for TEM analyses. The IOM was first extracted from the Orgueil chondrite by demineralization using HCl and HF acid to remove silicates, carbonates, sulfates, and other minerals (Robert & Epstein 1982; Orthous-Daunay et al. 2013). The resulting product was sliced by cryo-ultramicrotomy in order to obtain electron transparent thin foils of IOM.

Vibrational-EELS microscope working conditions. Vibrational-EELS acquisitions were conducted on an aberration corrected and monochromated NION Chromatem STEM,

located at the Laboratoire de Physique des Solides in Orsay. In order to minimize beam damage, the Chromatem microscope was operating at 100 kV. Spectrum images were acquired with a 15 mrad convergence semiangle, a low beam current (<10 pA), and a dwell time of 10 ms. The spectra were recorded at an energy dispersion of 2.7 meV/channel and the signal was collected by the Merlin direct electron detector Medipix3. These microscope settings allowed to reach an FWHM of about 15 meV (i.e., 120 cm^{-1} spectral resolution). As we probe phonon modes, delocalization of the signal occurs, which degrades the spatial resolution. Delocalization is wavelength dependent. At $10\text{ }\mu\text{m}$ (i.e., 130 meV), a residual signal can be detected up to approximately 100 nm (Egerton et al. 2023). At smaller wavelengths, the resolution improves to approximately 10 nm at $2\text{ }\mu\text{m}$. Ryugu data were acquired in a cryogenic sample holder at liquid nitrogen temperature, while other acquisitions were obtained at room temperature (RT). The scanned areas are about $500*500\text{ nm}^2$ large, and the resulting signal was summed to increase the signal-to-noise ratio (S/N). For each RT acquisition, several frames of the same area were collected, aligned and summed. The zero-loss-peak (ZLP) contribution has been removed by fitting a log-polynomial function to the data (Appendix A—Figure 4).

STEM-HAADF and STEM-EDXS microscope working conditions. TEM was performed on an FEI TITAN Themis 300 STEM located at the Michel-Eugène Chevreul Institute, University of Lille. The STEM is equipped with a high brightness Schottky FEG and a monochromator. High-angle annular dark field (HAADF) imaging was acquired using a 300 kV electron beam, a convergence semiangle of 18 mrad, and a 80 pA probe current. For the STEM-EDXS mapping, a Thermo Fisher super-X windowless four quadrant silicon drift detection was used, at 300 kV, with a 10 mrad convergence semiangle and a probe current ranging from 250 to 400 pA. To minimize electron beam damage on the samples, short dwell times per pixel were maintained ($2\text{--}8\text{ }\mu\text{s pixel}^{-1}$). Quantification of the EDXS data was conducted by applying the absorption correction and using k-factors for major elements (O, Fe, Mg, Al, S, Ca, and K), experimentally determined with mineral standards.

Scanning transmission X-rays microscopy (STXM) at the Fe $L_{2,3}$ edge. STXM data were collected at the SOLEIL synchrotron using the Scanning Transmission X-Ray Microscope of the HERMES beamline (Belkhou et al. 2015). Energy calibration was done using an internal hematite standard. STXM data were extracted from image stacks collected at energy increments of 0.15 eV over the Iron $L_{2,3}$ edge energy range (703–715 eV). Pixel size is $\sim 30*30\text{ nm}^2$ and the dwell time was set at 1 ms pixel^{-1} to prevent irradiation damage (Wang et al. 2009). Alignment of stacks images, extraction of STXM spectra, and valency quantification were performed using the open-source Python software package HyperSpy (de la Peña et al. 2017). Quantification of the iron valency was performed based on the protocol and calibration established by Le Guillou et al. (2015), following the work of Bourdelle et al. (2013). At each pixel of the hyperspectral data set, a background (680–700 eV) and a double arctangent function are fitted and subtracted to consider the iron content. The spectra are then integrated over ranges specific to the Fe^{2+} and Fe^{3+} absorption energies. These integrated values are then derived into valency values using the standard-based calibration. As a result, quantified valency maps are produced, and averaged spectra can be displayed. In order to avoid any

potential electron beam damage due to TEM observations, STXM analyses were conducted prior to electron microscopy.

Micro-FTIR spectroscopy. The infrared spectra of bulk Ryugu and Orgueil as well as Orgueil IOM were measured with a Bruker Hyperion 3000 infrared microscope. Spectra were measured in transmission and obtained by putting the diamond window in a custom-made environmental chamber, which enables us to expose the sample to a secondary vacuum, and an elevated temperature if needed (up to 100°C), as described in previous studies (Phan et al. 2022).

Data processing. The electron and X-ray microscopy data were processed using the open-source software Python package HyperSpy (de la Peña et al. 2017).

Data availability. Both vibrational-EELS raw and processed data are available. They are accompanied by a Jupyter Notebook describing the data processing presented in the Appendix (Figure 4) (available here: doi:10.5281/zenodo.8413674)

3. Results

3.1. Ryugu Grains Surface Analyses by Scanning Electron Microscopy

Scanning electron microscopy (SEM) observations of Ryugu grains surfaces generally show a rough aspect, due to the presence of phyllosilicates (Figure 1(a)). However, a small fraction of the Hayabusa2 sample collection, around 6%–7%, displays textures attributed to space-weathering effects (Noguchi et al. 2022). It includes thin smooth surfaces, that have been interpreted as the result of solar wind irradiation, and melt silicate layers, containing vesicles (Figure 1(b)). The latter morphology resembles to melt deposits generated by micrometeorites impacts (Noguchi et al. 2022). Samples returned by the Hayabusa2 space mission offer the first opportunity to study these space-weathering features on a hydrated and carbonaceous asteroid.

3.2. Cross-sectional Imaging of Space-weathered Grains by STEM

Thin sections containing melt layers were extracted using FIB. STEM-High Angle Annular Dark Field (STEM-HAADF) imaging of space-weathered grains allow determining the melt layer thickness, which can reach a few microns (up to $3\text{ }\mu\text{m}$). The interface between this layer and the unweathered underlying matrix is sharp and contains a high density of vesicles (Figure 2(a)). These layers also contain numerous rounded nanosulfides, ranging in size from a few tens of nanometers to a few hundred nanometers. STEM-EDXS analysis reveals that the composition of the silicate in the space-weathered layers resembles that of the underlying matrix (Figure 2(d)), but is depleted in carbon (Figure 2(c)), and shows a slight enrichment in Fe, as well as a Si depletion (Figure 2(d)). STXM Fe oxidation was determined for both the phyllosilicate-rich matrix and the melt layer. This analysis revealed that while a lot of Fe^{3+} is initially present in the phyllosilicate-rich matrix ($\sim 50\%\text{--}75\%\text{Fe}^{3+}/\sum\text{Fe}_{\text{total}}$), iron atoms are reduced to Fe^{2+} in the melt layers (Appendix—Figure 5).

3.3. Ryugu Space-weathered Surface Spectral Signature in the MIR

Our vibrational-EELS data set covers the MIR region ($600\text{--}4000\text{ cm}^{-1}$, $2.5\text{--}12\text{ }\mu\text{m}$), i.e., the 80–500 meV energy range (Figure 3(a)). Spectra from CI chondrite Orgueil and reference phyllosilicates samples (saponite and serpentine) all

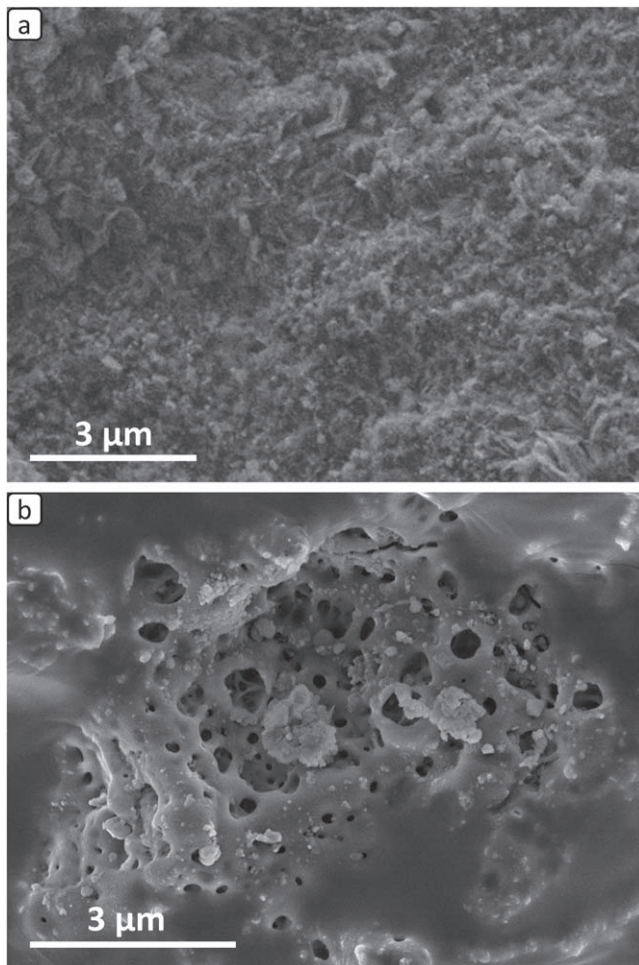


Figure 1. (a) SEM-secondary electrons image of an unweathered Ryugu grain showing a rough surface texture (sample C0105-034-010a); (b) vesiculated surface (melt layer) of space-weathered grains (C0105-034-001d).

show the dominant Si–O stretching mode at ~ 130 meV (i.e., 1000 cm^{-1} , $10\ \mu\text{m}$; Figure 3(a)). Compared with FTIR spectra, this peak is broadened and slightly shifted to lower wavelengths. This shift is constant within our data set and may be an artifact resulting from the background subtraction. Ryugu vibrational-EELS spectra measured in the space-weathered layer and in the matrix both exhibit the dominant Si–O peak, but at distinct positions. In the melt layer, this mode is present at lower energy loss (126 meV or $9.84\ \mu\text{m}$) compared to all other vibrational-EELS spectra (130 meV or $9.54\ \mu\text{m}$). The Mg–OH stretching mode at 457 meV (i.e., 3690 cm^{-1} , $2.71\ \mu\text{m}$) is observed in all phyllosilicate-bearing samples (Figure 3(b)) and is only barely visible in saponite. This discrepancy might be attributed to a lower number of hydroxyl groups per formula unit compared to serpentine. Remarkably, the feature is totally absent in the Ryugu melt layer, whereas it is clearly visible in the adjacent underlying matrix, albeit slightly shifted to lower energy losses when compared to Orgueil and reference phyllosilicate samples. FTIR and EELS spectra of IOM from Orgueil display a broad feature between 150 and 215 meV (i.e., $1250\text{--}1750\text{ cm}^{-1}$, $5.8\text{--}8\ \mu\text{m}$) corresponding to C=O, C=C stretching and CH_2 bending modes. At around 365 meV (i.e., 2950 cm^{-1} , $3.4\ \mu\text{m}$), the C–H_n stretching modes are also present. Ryugu’s melt layer spectrum does not show contributions from organics, in agreement with the

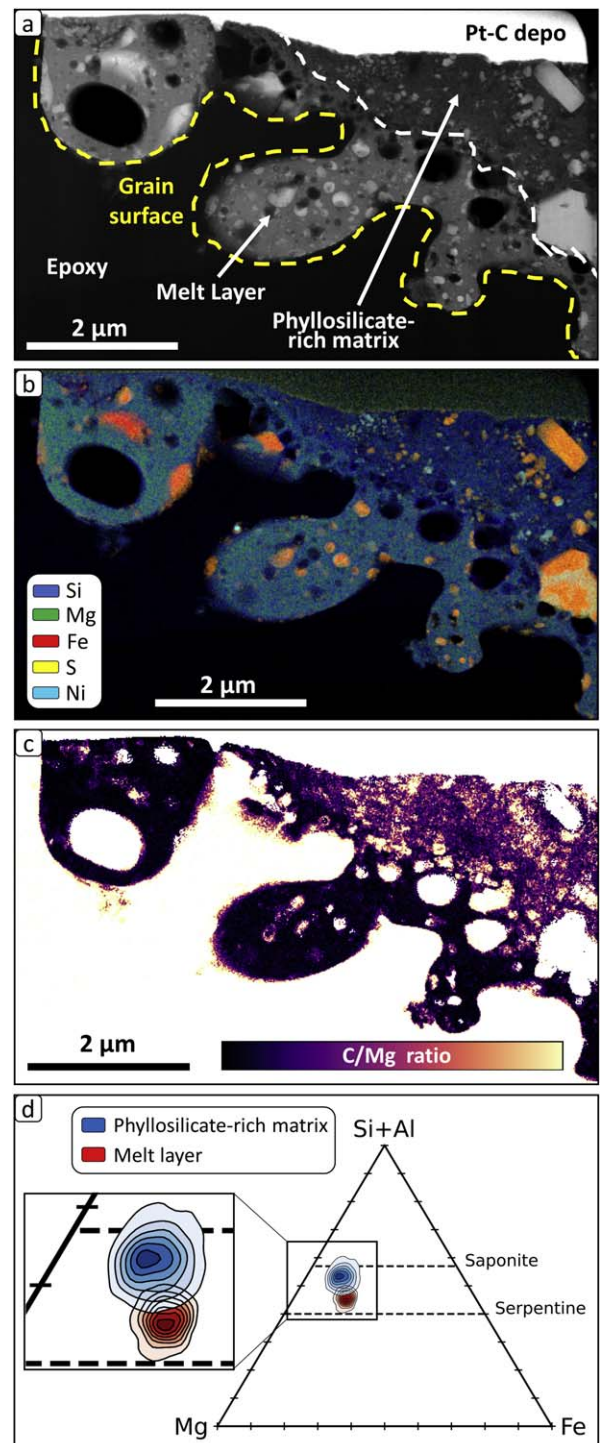


Figure 2. FIB cross section of a Ryugu grain surface (A0058-C2001-02). (a) STEM-HAADF image showing a surface covered by glassy globules containing vesicles and rounded Fe-Ni-sulfides. The interface with the pristine phyllosilicate basement is highlighted by a dashed white line (modified after Noguchi et al. 2022); (b) STEM-EDXS X-Ray lines intensity color map of the sample, allowing the identification of the Si, Mg, Fe, S, and Ni rich phases; (c) qualitative evolution of the C/Mg ratio, based on the STEM-EDXS X-Ray lines intensities, illustrating the low level of C in the glassy layer; (d) (Si+Al)-Mg-Fe ternary diagram of quantified STEM-EDXS silicate material data, where the A0058-C2001-02 melt layer is isolated from the unweathered phyllosilicate-rich matrix (pixel size = 17 nm).

absence of carbon observed by STEM-EDXS (Figure 2(c)). In Ryugu matrix spectra, a contribution from the vibrational mode of CO_2 molecules is visible at ~ 290 meV (i.e., 2350 cm^{-1} ,

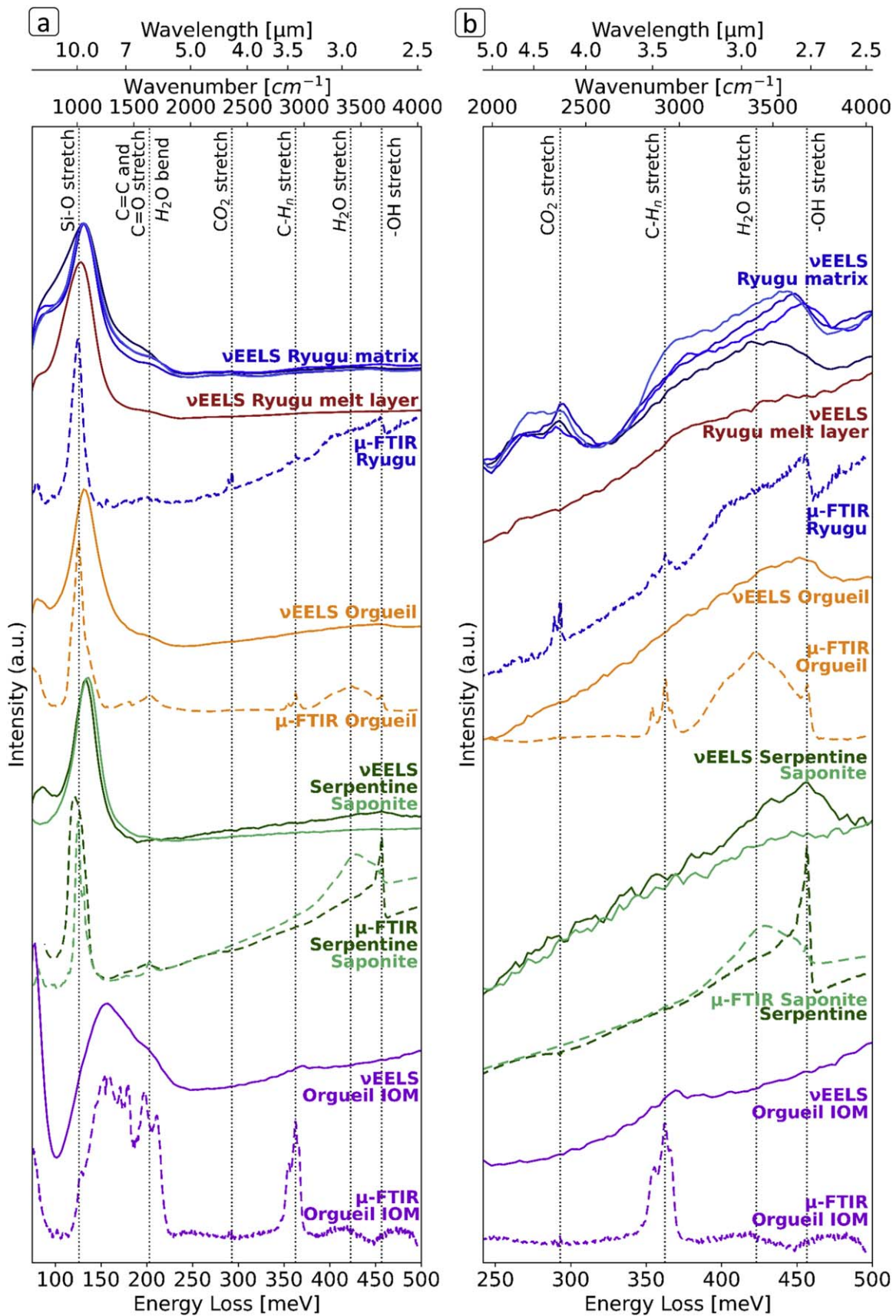


Figure 3. Vibrational-EELS spectra of Ryugu space-weathered (A0058-C2001-02) and unweathered samples (darkest blue line: A0058-C2001-02, other blue lines: C0105-034-010b01), compared with μ -FTIR data from Ryugu (A0104), analogs (Orgueil matrix and IOM), and phyllosilicate reference samples (serpentine and saponite): (a) 80–500 meV range (i.e., 600–4000 cm^{-1}), normalized to the absorption intensity of the Si–O band. (b) 240–500 meV range (i.e., 2000–4000 cm^{-1}), normalized arbitrarily for visualization purposes of the different vibrational modes (i.e., -OH and CH_n stretching modes).

4.25 μm), which could potentially arise from electron beam damage of the C-rich materials initially present in the matrix.

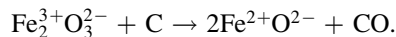
4. Discussion

4.1. Space-weathering Features in Ryugu

Following Noguchi et al. (2022, 2023), our results show that space-weathering features on Ryugu samples consist of an amorphous silicate layer with a thickness extending up to a few microns. Its morphology suggests a deposition of a micrometric melted silicate droplet on the asteroid surface (Figure 1(b)). These layers contain numerous nanometer sized vesicles, indicating degassing of the hot material (Figures 1(b), 2). Simulated microcratering experiments on aqueously altered carbonaceous chondrites and reference phyllosilicates using nanosecond and femtosecond pulsed lasers described the formation of identical vesiculated structures, trapped within a melted layer of silicate material (Thompson et al. 2020; Hallatt et al. 2022). Additionally, the melt layers contain numerous rounded nanosulfides (Figure 2) finely dispersed in the silicate glass and even sometimes concentrated at the interface with the phyllosilicate matrix, hinting to the possibility of locally reaching temperatures above 1200°C, the melting point of iron sulfides (Hsieh et al. 1982). This scenario led to the formation of a silicate-sulfides emulsion. The presence of nanosulfides, vesicles, and the glassy nature of the silicate suggest that the melt cooled rapidly after the impact, likely within a nanosecond (Kissel & Krueger 1987), preventing the coalescence and growth of sulfides and vesicles.

4.2. Spectral Signature of Space-weathering Features in Ryugu

Thanks to vibrational-EELS, we are able for the first time to document at the nanoscale the MIR spectral signature modifications due to this high-temperature event. The present results reveal the loss of structural -OH groups and organic matter in the space-weathered layers (Figure 3). In addition, the shift of the Si–O stretching band to higher wavelengths observed in space-weathered layers spectrally strengthen the interpretation of a high-temperature event, as this peak is sensitive to the composition and thermal history of the silicate (Beck et al. 2014). Brunetto et al. (2020) highlighted similar shifts to higher wavelengths after experimentally irradiating Ryugu analogs. STXM results show that the Fe^{3+} present in the unweathered phyllosilicate-rich matrix changes to Fe^{2+} in the melted silicate layer (Noguchi et al. 2022). Since STEM-EDXS and vibrational-EELS analyses reveal a substantial loss of organics in the melt layer, we can infer that the initial carbon present in Ryugu’s matrix may have acted as a reducing agent during the high-temperature event. This is likely to have caused the degassing of carbon monoxide following the reaction:



4.3. Link with Remote Observations

Being able to combine textural and spectral observation allows for interpreting the asteroidal surface properties at larger scales. We showed here that space-weathering processes can lead to the dehydroxylation and dehydration of the very surface of grains exposed to the space environment. The direct consequence is that the surface of phyllosilicate-dominated asteroids may appear “dry” based on infrared observation in the 3 μm region. The fraction of hydrated asteroids derived from telescopic observations may therefore be taken as a minimum.

Similarly, the presence of visible optical signature of hydration at 0.7, 0.9, and 1.1 μm observed on Mighei-grouped chondrites and a significant fraction of C-type asteroids, may also be impacted by the reduction of Fe^{3+} into Fe^{2+} in the space-weathered layers. Lastly, the presence of organic compounds of C-type asteroids can be searched for with 3.4–3.5 μm C–H modes, but they remain undetected on these objects with the exception of 1-Ceres (De Sanctis et al. 2015). Although they are detected in the reflectance spectra of meteorites, the general lack of organic absorption mode observed among C-type asteroids can be explained by the reduction and loss of organic carbon in the space-weathered layer.

5. Conclusions

Our work has shown that the two main absorption signatures used to search for primitive asteroids, i.e., hydration and organics, might be easily masked by space weathering. This could be taken by the community to develop other diagnostic tools, such as higher-wavelength spectroscopy, which have deeper penetration depth and could thus be able to probe the material beneath the melted surfaces of asteroids. These unique observations allowed by sample returned mission and a remote versus laboratory comparison pave the way to interpret other spectral data sets acquired on asteroid populations. The ongoing development of vibrational-EELS, used here for the first time for space-weathering investigations, combined with nanostructural (STEM-HAADF) and chemical (STEM-EDXS) analysis techniques will soon give the opportunity to further study the spectral influence of space-weathering effects on other C-type asteroid samples, with NASA’s OSIRIS-REX sample return mission from asteroid Bennu (Lauretta et al. 2019; DellaGiustina et al. 2020; Hanna et al. 2024). As the new generation of telescopes, such as the promising James Webb Space Telescope, is now able to probe the small airless bodies of the solar system in the infrared (Rivkin et al. 2016; Thomas et al. 2016), improving our knowledge about space-weathering effects in this spectral range is fundamental to correctly classify asteroids.

Acknowledgments

The Hayabusa2 project has been developed and led by JAXA in collaboration with Deutsches Zentrum für Luft- und Raumfahrt (DLR) and Centre national d’études spatiales (CNES), and supported by NASA and Australian Space Agency (ASA). We thank all the members of the Hayabusa2 project for their technical and scientific contributions. This work was carried out on the electron microscopy facility of the Advanced Characterization Platform of the Chevreul Institute, University of Lille—CNRS. This project has been funded by ISITE ULNE and the “Métropole Européenne de Lille” through the “TEM-Aster project,” the LARCAS ANR (Reference No. SAN-22199). It has also been funded by in part by the National Agency for Research (ANR) under the program of future investment TEMPOS-CHROMA-TEM (Reference No. ANR-10-EQPX-50). Micro-infrared spectroscopy was performed at the Institut de Planétologie et d’Astrophysique de Grenoble (IPAG). European Union’s Horizon 2020 research and innovation program under Grant Agreements No. 823717 (ESTEEM3). The Chevreul Institute is thanked for its help in the development of this work through the CHEMACT project supported by the “Ministère de l’Enseignement Supérieur de la Recherche et de l’Innovation,” the region “Hauts-de-France”

and the “Métropole Européenne de Lille.” JSPS KAKENHI grant numbers related to this study are 19H00725, 19K0094, and 21H05424. This research was supported by the H2020 European Research Council (ERC) (SOLARYS ERC-CoG2017-771691). We acknowledge the funding by the Spanish University Ministry and Next Generation EU through a Margarita Salas fellowship. We acknowledge SOLEIL for provision of synchrotron radiation facilities and we would like to thank R.Belkhou, S.Stanescu, and S.Swaraj for assistance in using beamline “Hermes.”

Appendix A Vibrational-EELS Data Processing

Remove the contribution of the ZLP in an EELS spectrum is nontrivial as no mathematic model describes the phenomenon with an extreme precision. To approximate the ZLP tail contribution, we used HyperSpy (de la Pena et al. 2017) to fit a

log-polynomial function to the nonbinned data (Figure 4(a)).

$$f(x) = A * e^{b * \log|x - x_0|} \quad (\text{A1})$$

A, b, and x0 parameters were set free. The fitting ranges were chosen to avoid the contribution of peaks from the data during the fit (Figure 4(b)). For silicate-rich samples, the fit was performed on the ranges [70–80] and [230–1000] meV. For C-rich samples, the fit was performed on the ranges [70–100] and [500–1000] meV. After the fit (Figure 4(c)), the model intensity is subtracted to the data, in order to remove the ZLP contribution (Figure 4(d)). The fit is performed pixel per pixel on the data. The data are binned after the ZLP correction. The processing final objective is to obtain qualitatively comparable data.

Data and processing routine available here: doi:[10.5281/zenodo.8413674](https://doi.org/10.5281/zenodo.8413674).

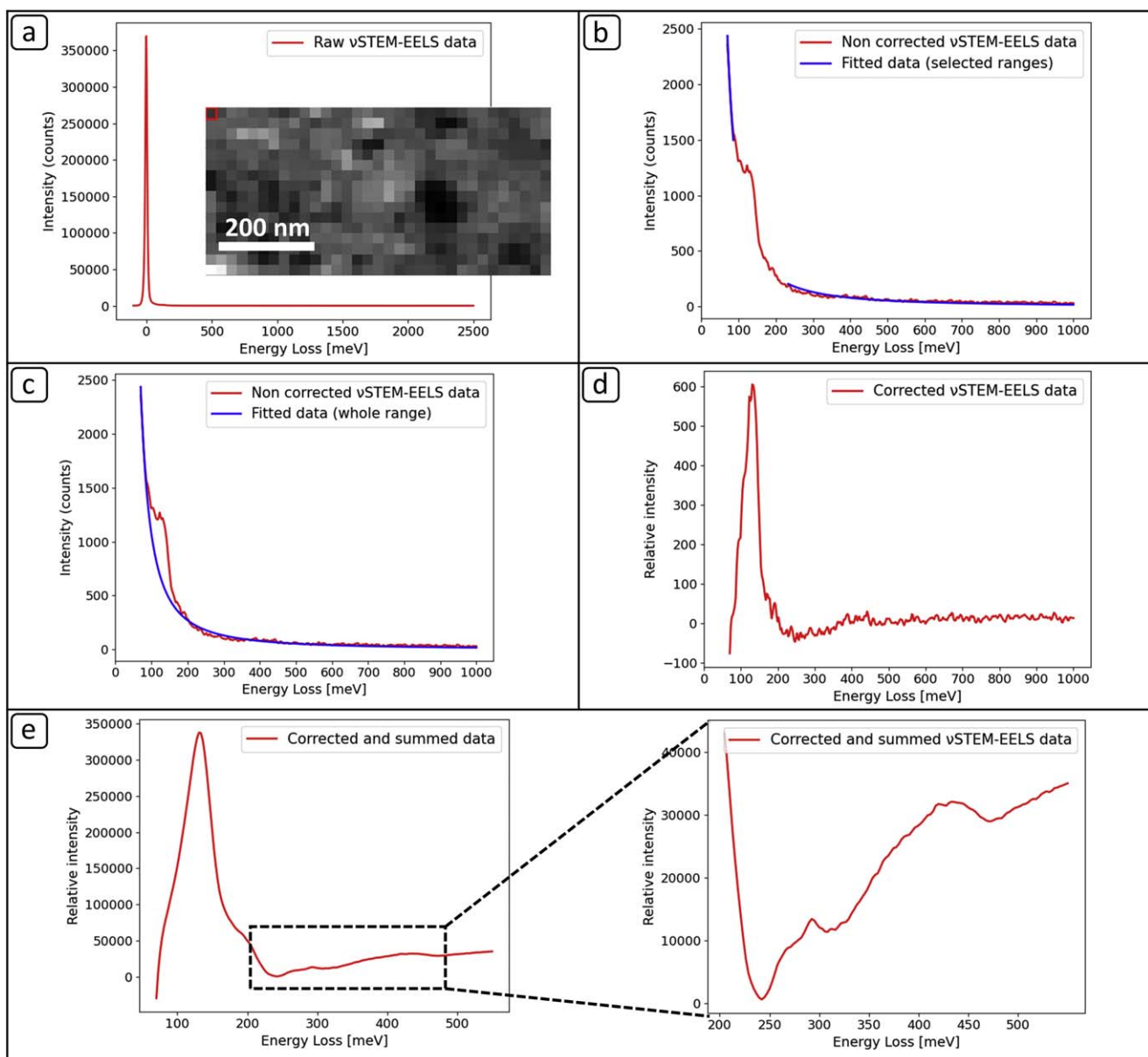


Figure 4. ZLP correction data processing details: (a) examples of a vibrational-EELS Spectrum-Image (pixel [0,0]) from a Ryugu phyllosilicate-rich matrix data (sample A0058-C2001-02); (b) fit performed pixel per pixel on the range [70–80] and [230–1000] meV; (c) the whole model after the fit; and (d) the final signal after subtracting the fitted model to the data. (e) The signal is summed to enhance the S/N.

Appendix B

STXM Study of Ryugu's Iron Oxidation State

Figure 5 summarizes the different STXM measurements performed at the $Fe\ L_{2,3}$ edge on Ryugu FIB sections.

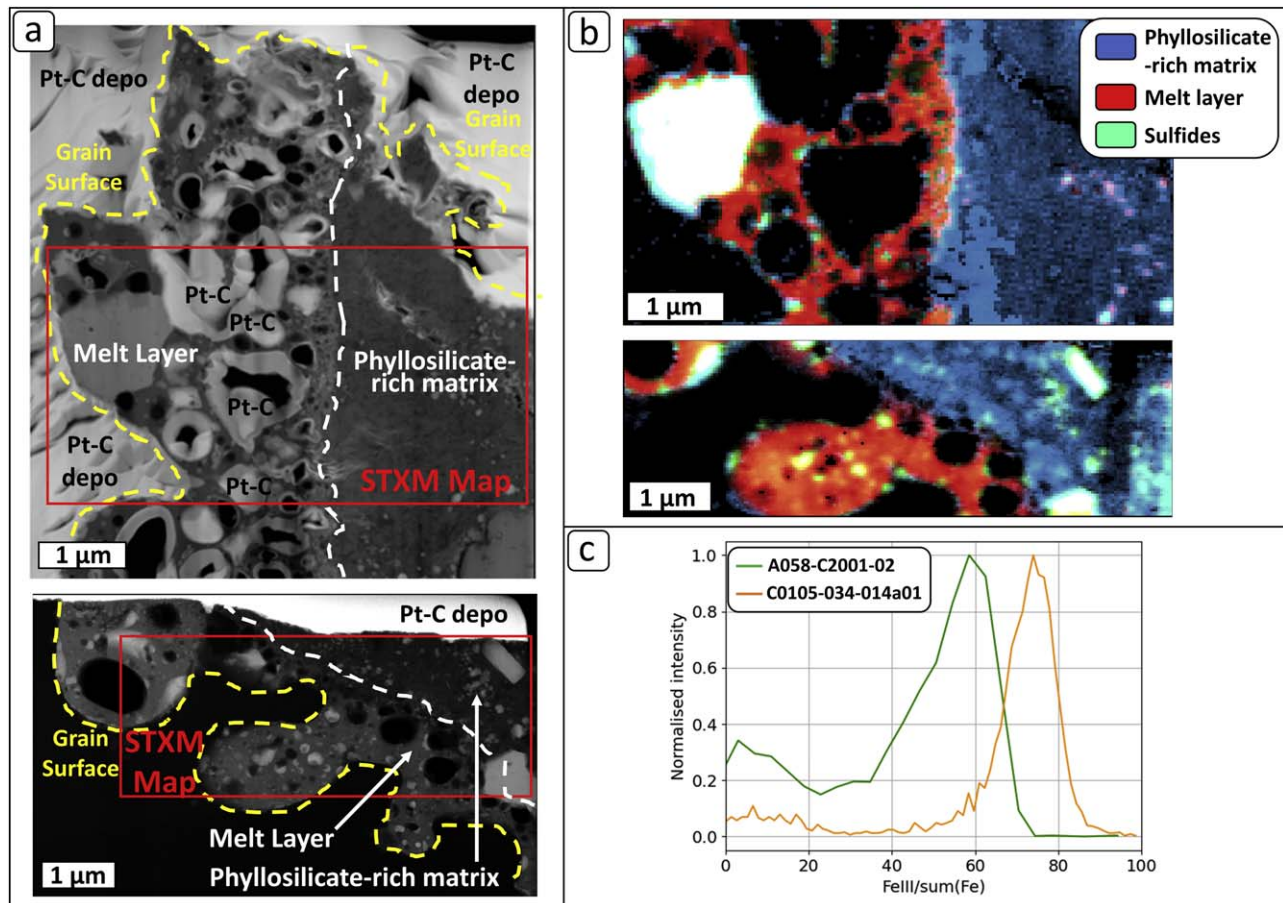


Figure 5. STXM studies of the Fe-oxidation state: (a) STEM-HAADF image of the FIB sections analyzed, showing a large space-weathered (melt layer) areas (C0105-034-014a01 and A0058-C2001-02), Pt-C deposition was performed inside the vesicles of C0105-034-014a01 for FIB thinning purposes. (b) STXM maps showing the spatial repartition of different Fe-oxidation states. (c) Histogram of the Fe^{3+} distribution in both FIB sections, showing a heterogeneity of the phyllosilicate-rich matrix Fe oxidation state.

Appendix C Vibrational-EELS and FTIR Spectra Comparison

In order to be able to directly compare the FTIR and EELS data that have different spectral resolutions, the FTIR spectrum was broadened using a Gaussian filter. It results in spectra that resemble the vibrational-EELS spectra position and shape (Figure 6). The -OH stretching band, initially found at $2.71 \mu\text{m}$ (i.e., 457 meV) in

the FTIR data, shifts to higher wavelengths when broadened, adopting a similar position to that in EELS (i.e., 450 meV or $2.76 \mu\text{m}$). This shift results from the convolution of the different modes present in this spectral region such as the C-H_n and H₂O stretching modes. The Si-O stretching band ($10 \mu\text{m}$) of the broadened FTIR spectrum, however, remains shifted and thinner than the EELS ones.

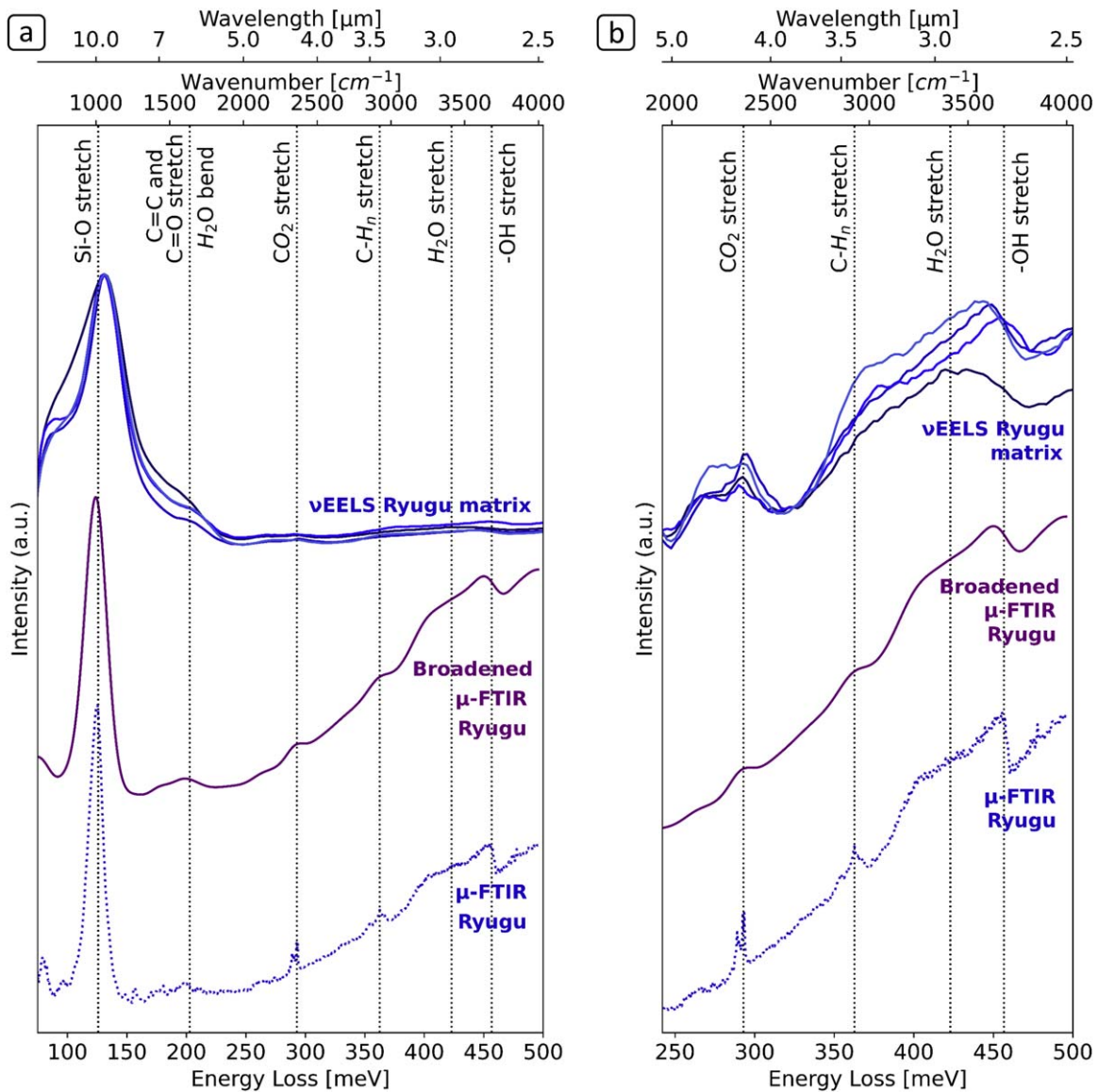


Figure 6. Vibrational-EELS spectra of Ryugu phyllosilicate-rich matrix compared with FTIR data, and broadened FTIR data. Broadening is performed using a Gaussian filter to match the EELS spectral resolution (i.e., 15 meV). (a) 80–500 meV range (i.e., 600–4000 cm^{-1}) and (b) 240–500 meV range (i.e., 2000–4000 cm^{-1}).

Appendix D**Sample A0058-C2001-02 Supplementary Information**

Phyllosilicates lying just below the melt layer interface show a less intense stretching -OH feature (Figure 3(b)—darkest blue line). It may result from the electron delocalization effects that

detect the surrounding dehydroxylated melt layer. Depending on the wavelength, this signal delocalization is known to range between a few tens of nanometers to a hundred nanometers. Figure 7 summarizes the locations of the different acquisitions on this sample.

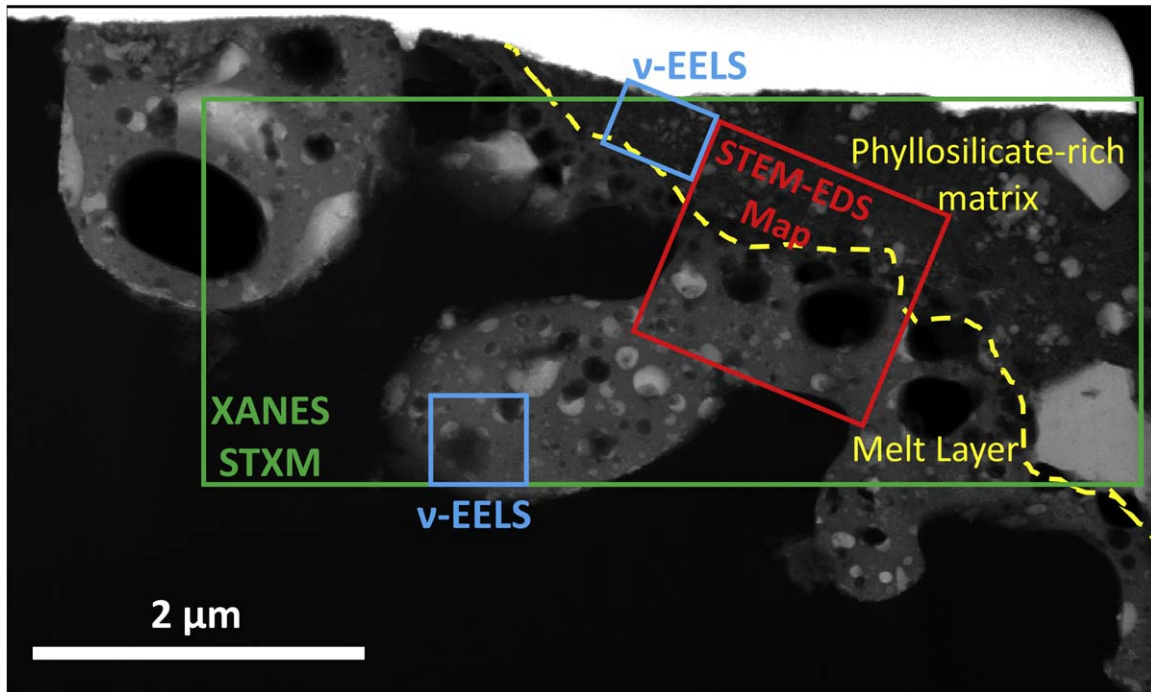






Figure 7. STEM-HAADF image of FIB Section A0058-C2001-02 (modified after Noguchi et al. 2022). Localization of the different experimental techniques and acquisitions conducted on the sample.

ORCID iDs

Sylvain Laforet  <https://orcid.org/0000-0002-8302-7123>
 Daniel Hallatt  <https://orcid.org/0000-0002-4426-9891>
 Takaaki Noguchi  <https://orcid.org/0000-0001-7211-2595>
 Hisayoshi Yurimoto  <https://orcid.org/0000-0003-0702-0533>

References

- Beck, P., Garenne, A., Quirico, E., et al. 2014, *Icar*, **229**, 263
 Belkhou, R., Stanescu, S., Swaraj, S., et al. 2015, *JSynR*, **22**, 968
 Bourdelle, F., Benzerara, K., Beyssac, O., et al. 2013, *CoMP*, **166**, 423
 Brunetto, R., Lantz, C., Nakamura, T., et al. 2020, *Icar*, **345**, 113722
 Brunetto, R., Loeffler, M. J., Nesvorný, D., Sasaki, S., & Strazzulla, G. 2015, in *Asteroids IV*, ed. P. Michel, F. E. DeMeo, & W. F. Bottke (Tucson, AZ: Univ. of Arizona Press), 597
 Chapman, C. R. 2004, *AREPS*, **32**, 539
 Colliex, C. 2022, *EPJAP*, **97**, 38
 Dartois, E., Kebukawa, Y., Yabuta, H., et al. 2023, *A&A*, **671**, A2
 Dazzi, A., & Prater, C. B. 2017, *ChRv*, **117**, 5146
 de la Peña, F., Ostasevicius, T., Fauske, V. T., et al. 2017, *MiMic*, **23**, 214
 De Sanctis, M. C., Ammannito, E., Raponi, A., et al. 2015, *Natur*, **528**, 241
 DellaGiustina, D. N., Burke, K. N., Walsh, K. J., et al. 2020, *Sci*, **370**, eabc3660
 Egerton, R., Wang, Y., & Crozier, P. A. 2023, *Spatial Resolution in Alooof EELS* (Oxford: Oxford Univ. Press)
 Hage, F. S., Radtke, G., Kepaptsoglou, D. M., Lazzeri, M., & Ramasse, Q. M. 2020, *Sci*, **367**, 1124
 Hallatt, D., Leroux, H., Dubois, E., & Braud, F. 2022, *LPSC*, **2678**, 2568
 Hanna, R. D., Hamilton, V. E., Haberle, C. H., et al. 2024, *Icar*, **408**, 115809
 Hapke, B. 2001, *JGRE*, **106**, 10039
 Herman, A. 2013, *Reviews in Theoretical Science*, **1**, 3
 Hsieh, K.-C., Chang, Y. A., & Zhong, T. 1982, *Bulletin of Alloy Phase Diagrams*, **3**, 165
 Ito, M., Tomioka, N., Uesugi, M., et al. 2022, *NatAs*, **6**, 1163
 Jokisaari, J. R., Hachtel, J., Hu, X., et al. 2018, *MiMic*, **24**, 422
 Kebukawa, Y., Kobayashi, H., Urayama, N., et al. 2019, *PNAS*, **116**, 753
 Keller, L. P., & McKay, D. S. 1997, *GeCoA*, **61**, 2331
 Kissel, J., & Krueger, F. R. 1987, *ApPhA*, **42**, 69
 Kitazato, K., Milliken, R. E., Iwata, T., et al. 2019, *Sci*, **364**, 272
 Kitazato, K., Milliken, R. E., Iwata, T., et al. 2021, *NatAs*, **5**, 246
 Krivanek, O. L., Lovejoy, T. C., Dellby, N., et al. 2014, *Natur*, **514**, 209
 Lauretta, D., DellaGiustina, D., Bennett, C., et al. 2019, *Natur*, **568**, 55
 Le Guillou, C., Changela, H. G., & Brearley, A. J. 2015, *E&PSL*, **420**, 162
 Leroux, H., Le Guillou, C., Marinova, M., et al. 2023, *M&PS*,
 Lodders, K. 2003, *ApJ*, **591**, 1220
 Mahlke, M., Carry, B., & Mattei, P.-A. 2022, *A&A*, **665**, A26
 Mathurin, J., Dartois, E., Pino, T., et al. 2019, *A&A*, **622**, A160
 Mathurin, J., Deniset-Besseau, A., Bazin, D., et al. 2022, *JAP*, **131**, 010901
 Matsumoto, T., Noguchi, T., Miyake, A., et al. 2024, *NatAs*, **8**, 207
 Matsumoto, T., Noguchi, T., Tobimatsu, Y., et al. 2021, *GeCoA*, **299**, 69
 Matsuoka, M., Kagawa, E.-i., Amano, K., et al. 2023, *ComEE*, **4**, 335
 Michel, P., Ballouz, R.-L., Barnouin, O. S., et al. 2020, *NatCo*, **11**, 2655
 Nakamura, T., Matsumoto, M., Amano, K., et al. 2023, *Sci*, **379**, eabn8671
 Noguchi, T., Kimura, M., Hashimoto, T., et al. 2014, *M&PS*, **49**, 188
 Noguchi, T., Matsumoto, T., Miyake, A., et al. 2022, *NatAs*, **7**, 170
 Noguchi, T., Matsumoto, T., Miyake, A., et al. 2023, *M&PS*,
 Noguchi, T., Nakamura, T., Kimura, M., et al. 2011, *Sci*, **333**, 1121
 Orthous-Daunay, F.-R., Quirico, E., Beck, P., et al. 2013, *Icar*, **223**, 534
 Phan, V. T., Rebois, R., Beck, P., et al. 2022, *M&PS*, **57**, 3
 Phan, V. T., Rebois, R., Beck, P., et al. 2023, *IJCG*, **267**, 104196
 Pieters, C. M., & Noble, S. K. 2016, *JGRE*, **121**, 1865
 Pieters, C. M., Taylor, L. A., Noble, S. K., et al. 2000, *M&PS*, **35**, 1101
 Pilorget, C., Okada, T., Hamm, V., et al. 2022, *NatAs*, **6**, 221
 Rivkin, A. S., Campins, H., Emery, J. P., et al. 2015, *Asteroids IV* (Tucson, AZ: Univ. of Arizona Press), 65
 Rivkin, A. S., Marchis, F., Stansberry, J. A., Takir, D., & Thomas, C. 2016, *PASP*, **128**, 018003
 Robert, F., & Epstein, S. 1982, *GeCoA*, **46**, 81
 Stroud, R., Lagos, M. J., & Batson, P. E. 2019, *LPSC*, **2132**, 2259
 Thomas, C. A., Abell, P., Castillo-Rogez, J., et al. 2016, *PASP*, **128**, 018002
 Thompson, M. S., Christoffersen, R., Zega, T. J., & Keller, L. P. 2014, *EP&S*, **66**, 89
 Thompson, M. S., Morris, R. V., Clemett, S. J., et al. 2020, *Icar*, **346**, 113775
 Tsuda, Y., Saiki, T., Terui, F., et al. 2020, *AcAau*, **171**, 42
 Vollmer, C., Leitner, J., Kepaptsoglou, D., et al. 2019, *M&PS*, **55**, 1293
 Wang, J., Botton, G. A., West, M. M., & Hitchcock, A. P. 2009, *JPCB*, **113**, 1869
 Watanabe, S., Hirabayashi, M., Hirata, N., et al. 2019, *Sci*, **364**, 268
 Yada, T., Abe, M., Okada, T., et al. 2022, *NatAs*, **6**, 214
 Yessiltas, M., Glotch, T. D., & Sava, B. 2021, *NatSR*, **11**, 11656
 Yokoyama, T., Nagashima, K., Nakai, I., et al. 2023, *Sci*, **379**, abn7850